Optical Satellite Orbit Determination from Geographically Dispersed Sensors

Luke W. Renegar * and Brian C. Gunter †
Georgia Institute of Technology, Atlanta, GA 30363

Because of their relative simplicity, optical tracking systems are potentially much more cost-effective than radar for tracking resident space objects (RSOs); however, they suffer from a key drawback compared to radar in that they cannot provide range information. One way of overcoming this limitation is by triangulating the RSO's position using multiple geographically diverse sensors. This paper presents a comparison of using triangulation techniques against using observations from similar ground station arrangements in more traditional sensor fusion techniques, such as Kalman Filtering. The influence of the geographical layout of the sensors on the quality of the orbit solution is discussed, as is the impact of the number of ground stations in the network. Performance comparisons are placed in the context of usefulness to RSO catalog maintenance, and the question of whether the improvements are operationally meaningful is explored.

Nomenclature

GD	=	geometric diversity
H	=	measurement sensitivity matrix
HA_L	=	local hour angle
K	=	Kalman gain
P	=	covariance
h	=	altitude
t	=	time
$\mathbf{x}$	=	state vector
$\mathbf{y}$	=	measurement vector
Φ	=	state transition matrix
Ω	=	solid angle
α	=	topocentric right ascension (RA)

*Graduate Student, Guggenheim School of Aerospace Engineering, AIAA Student Member
†Associate Professor, Daniel Guggenheim School of Aerospace Engineering, AIAA Senior Member

β = azimuth

γ = elevation

δ = topocentric declination

ϵ = error

θ = sidereal time

ρ = range

ρ_x = x component of range

ρ_y = y component of range

ρ_z = z component of range

σ = standard deviation

ϕ = latitude

I. Introduction

Accurate knowledge of resident space object (RSO) orbits is of critical importance to many spaceflight operations. Not only is accurate orbit determination (OD) required by many satellites to effectively perform their missions, it underpins the space domain awareness (SDA) and space traffic management (STM) activities that enable all users of the near-Earth space environment to operate their vehicles safely and preserve an accessible space environment for future users. Historically, SDA and STM information has been distributed worldwide by the U.S. Department of Defense, who publish two-line element (TLE) sets for most RSOs at least 10 cm in size. The element sets for objects in low Earth orbit (LEO) are largely derived from observations from large, fixed radars, while the Ground-Based Electro-Optical Deep Space Surveillance (GEODSS) telescope system and a handful of deep-space search radars provide additional data for objects in higher orbits [1]. Because of the large number of objects tracked and the limitations of the sensors, many of which were built for missile defense early-warning purposes during the Cold War, TLE predictions are limited in accuracy to no more than a few kilometers in LEO. Moreover, accuracy begins to degrade drastically after a few days if the TLE is not updated with additional observations, particularly in the along-track direction due to uncertainties in the drag model [2, 3]. TLE errors in geostationary orbit (GEO) can be significantly worse, on the order of tens of kilometers [4, 5].

Satellite operators requiring more precise orbit solutions than the DoD TLEs rely on cued radars or satellite laser ranging stations, such as those provided by the International Laser Ranging Service, to provide additional data [6]. While these cued active sensors can provide orbit solutions accurate to the centimeter level based on azimuth, elevation, range, and range rate, they are expensive. Large radars can cost tens or hundreds of millions of dollars, while laser ranging stations can cost many hundreds of thousands of dollars. By contrast, optical systems are low-cost; a 0.5 m,

so-called Raven-class, telescope can be obtained from commercial suppliers for less than $80,000, and site requirements are relatively minimal. Multiple such systems have been deployed in support of academic SSA activities, both as individual telescopes and as a part of larger networks [7–9].

The key limitation of optical sensors, when compared against active sensors, is that a single optical sensor cannot measure range or range rate to an uncooperative RSO. Active sensors rely on measuring the propagation time of the signal between the sensor and the RSO, but this is unknown for a passive optical sensor. As a result, more optical observations are needed than radar or laser observations to uniquely determine an RSO's orbit, and a single optical observation will provide less information about an RSO track than a comparable radar or laser observation. Nevertheless, numerous examples of angles-only orbit determination algorithms exist, drawing on a heritage that dates to the astronomical work of Pierre Simon de Laplace in the 18th century, and optical tracking systems have seen use in operational SSA activities from the 1950's through the present day [1, 10–12].

While most of the classic orbit determination algorithms rely on processing an arc of observation vectors from a single site without *a priori* information, some recent efforts have focused on fusing optical observations from multiple sites, with or without *a priori* information, in order to provide more accurate orbit determination and overcome some of the inherent limitations of single-sensor optical systems. Given simultaneous observations of an RSO from two sites at a known distance apart, it is possible to infer the RSO's range to either of them using triangulation, sometimes even to sub-km accuracy, thus bypassing the principal limitation of optical sensors when compared to active sensor systems [13, 14]. As an alternative, the probability density functions (PDFs) resulting from near-simultaneous observations can be fused using various density rules. It has been suggested that, even without directly triangulating the range to the RSO, PDF fusion from near-simultaneous optical observations can reduce uncertainty in the RSO's position by a factor of 2.5-3 compared to single-sensor observations [15]. Other studies have considered how to best use single optical observations to reduce the propagated state uncertainty in an RSO's position and velocity given the nonlinear dynamics of the problem [3].

The present work presents a comparison of the available methods for using optical sensors for RSO catalog maintenance, with an emphasis on fusing observations from sensors in geographically dispersed locations. We explore what improvements in knowledge of an RSO's state can be be obtained using various configurations of optical tracking stations. Both simultaneous and non-simultaneous measurement models are considered, as are various orbital regimes. In view of the fact that uncertainties in the RSO's along-track position and velocity far exceed the uncertainties in other directions, we also explore the impact of ground station-RSO viewing geometries. By considering the frequency of observations needed to maintain certain bounds on the RSO's position covariance, we identify which ground station configurations are most helpful for maintaining custody of RSOs in particular orbital regimes. It is hoped that this work will be used to inform the selection of sites for new optical tracking systems, as well as the tasking of existing systems.

II. Measurement Models

Before considering the fusion of data from optical sensors, it is first useful to examine the nature of the data collected by an optical sensor tracking an RSO. Consider Fig. 1, with the RSO located at position **r** with respect to the Earth, and the ground station located at position **R**. As the sensor tracks the satellite, it points along vector $\rho = \mathbf{r} - \mathbf{R}$. A natural decomposition of ρ in an Earth-centered inertial (ECI) frame is the right ascension-declination coordinate system, given by Eqn. 1, where $\rho = ||\rho||$, α is the topocentric right ascension, and δ is the topocentric declination.

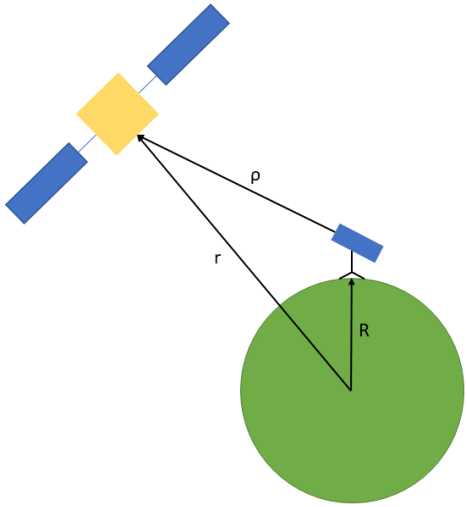

Fig. 1 Observation Geometry

$$\rho = \begin{bmatrix} \rho_x \\ \rho_y \\ \rho_z \end{bmatrix}_{ECI} = \begin{bmatrix} \rho \cos(\alpha) \cos(\delta) \\ \rho \sin(\alpha) \cos(\delta) \\ \rho \sin(\delta) \end{bmatrix}_{ECI} \tag{1}$$

$$\alpha = \arctan 2\left(\rho_y, \rho_x\right) \tag{2a}$$

$$\delta = \sin^{-1}\left(\rho_z / \rho\right) \tag{2b}$$

Because the right ascension and declination are defined in an inertial frame, while an Earth-based ground station is in a rotating frame, the question arises of how to measure these values. Modern telescopes generally use encoders to measure the rotation of the telescope mount's two axes; for equatorially-mounted telescopes, which have one axis parallel to the Earth's axis of rotation, the declination axis of the mount directly measures δ, while the right ascension axis measures the local hour angle HA_L, which is related to α by Eqn. 3, in which $\theta_L(t)$ is the local sidereal time,

which is the angle between the observatory's local meridian and the Greenwich meridian.

$$\alpha\left(t\right) = \theta_L\left(t\right) - HA_L\left(t\right) \tag{3}$$

Adopting the convention that $\tilde{x}$ refers to a measurement of some variable x, while $\hat{x}$ refers to an estimate of the true value, we arrive at the measurement model presented in Eqn. 4, where ϵ refers to a normally distributed error according to Eqn. 5.

$$\tilde{\delta} = \delta + \epsilon_\delta \tag{4a}$$

$$\tilde{\alpha} = \hat{\theta_L} - \tilde{HA_L} = \left(\theta_L + \epsilon_\theta\right) - \left(HA_L + \epsilon_{HA}\right) \tag{4b}$$

$$\epsilon_\delta \sim N\left(0, \sigma_\delta^2\right) \tag{5a}$$

$$\epsilon_{HA} \sim N\left(0, \sigma_{HA}^2\right) \tag{5b}$$

$$\epsilon_\theta \sim N\left(0, \sigma_\theta^2\right) \tag{5c}$$

This leaves the question of how to estimate the local sidereal time θ_L. Sidereal time is a linear function of the Earth's rotation, such that $\dot{\theta}$ is given by Eqn. 6. Thus, given the local sidereal time $\theta_{L,0}$ at some time t_0, θ_L can be estimated according to Eqn. 7. It is important to note that local clocks are seldom perfectly unbiased, and the clock time couples directly into $\tilde{\alpha}$. Thus, any bias in the clock translates directly to a bias in the $\tilde{\alpha}$ measurement, with 1 second of clock bias translating to a 15 arcsecond bias in $\tilde{\alpha}$. This bias can of course be estimated and removed during data reduction, but, while the rest of this work assumes $\beta_t = 0$ in order to maintained the unbiased estimator assumption, clock bias is a potentially significant source of error for precise measurements.

$$\dot{\theta}_L = \frac{360^\circ}{86\,164\,\mathrm{s}} \tag{6}$$

$$\hat{\theta}_L = \theta_{L,0} + \frac{360^\circ}{86\,164\,\mathrm{s}}\left(\hat{t} - t_0\right) = \theta_{L,0} + \frac{360^\circ}{86\,164\,\mathrm{s}}\left(t + \epsilon_t - t_0\right) \tag{7a}$$

$$\epsilon_t \sim N\left(\beta_t, \sigma_t\right) \tag{7b}$$

Telescopes with azimuth-elevation mounts reference their axes to the local horizon and zenith, with axes pointing to the south, east, and zenith of the telescope site; in this case, encoder measurements do not map directly to right ascension and declination coordinates. Given an azimuth angle β of a target with respect to north and an elevation angle γ of the

target above the local horizon, ρ can be represented in SEZ coordinates according to Eqn. 8. The transformation from the SEZ frame to the earth-centered inertial frame is given by Eq. 9, where ϕ represents the site's latitude [10]. Similar to the right ascension-declination case, errors in measured azimuth and elevation are assumed to be normally distributed about the true values with variances of σ_β^2 and σ_γ^2, respectively.

$$\underline{\rho} = \begin{bmatrix} -\rho\cos(\gamma)\cos(\beta) \\ \rho\cos(\gamma)\sin(\beta) \\ \rho\sin(\gamma) \end{bmatrix}_{SEZ} \tag{8}$$

$$\underline{\rho}_{ECI} = \begin{bmatrix} \cos(\theta_L) & -\sin(\theta_L) & 0 \\ \sin(\theta_L) & \cos(\theta_L) & 0 \\ 0 & 0 & 1 \end{bmatrix} \begin{bmatrix} \cos(\phi - 90°) & 0 & -\sin(\phi - 90°) \\ 0 & 1 & 0 \\ \sin(\phi - 90°) & 0 & \cos(\phi - 90°) \end{bmatrix} \underline{\rho}_{SEZ} \tag{9}$$

Another way of measuring α and δ is to use the star field in the background of the image. Various algorithms exist to analyze the relative position of stars in a frame and infer the position on the celestial sphere [16, 17]. The accuracy of this technique is typically limited by the angular extent of the pixels in the frame, so it can be quite precise. The error for this technique is not generally associated with one axis or the other, so it can be assumed that the errors are normally distributed with $\sigma_{ra} = \sigma_{dec}$.

III. The Orbital Estimation Problem

An RSO orbiting about the Earth can be modeled as a dynamical system with state $\mathbf{x}(t)$ propagating according to $\dot{\mathbf{x}}(t) = F(\mathbf{x}, t)$. At a minimum, $\mathbf{x}$ includes the six Cartesian position and velocity components, but it can also include certain parameters about the RSO that influence its trajectory, such as its ballistic coefficient or surface albedo. Even though those parameters are generally fixed for a particular RSO, their influence on an RSO's orbit allows them to be estimated. The orbit estimation problem consists of determining this state at some time t_0 to sufficient accuracy that the resulting propagation of the estimated state is still useful over some time period of interest. The orbit estimation problem has traditionally been divided into two categories: initial orbit determination, and orbit determination based on a priori information. The former attempts to determine an unknown orbit based on only observations, while the latter, which is the focus of this work, seeks to combine prior knowledge of the RSO's state at a time in the past with knowledge gained through observation at some later time.

As is more fully discussed in Section IV, the figure of merit for an orbit estimation technique in this work is the required revisit time for catalog maintenance. Since the force model $F(\mathbf{x}, t)$ is generally only an approximation of the

true dynamics, the uncertainty around the propagated state will increase over time; after a sufficient amount of time has passed, the state estimate becomes so uncertain as to not be useful (e.g., the tracking station cannot reliably acquire the satellite based on the predicted ephemeris). In order to prevent this, it is necessary to regularly observe the RSO and update the estimate of its state. Since making tracking observations of an RSO requires sensor time, a finite resource, orbit estimation procedures which require less frequent updates to maintain a certain level of uncertainty in the RSO's position are more useful than those which require more frequent updates.

A. Fusing Individual Observations with Batch Processing and Filtering

Perhaps the most well-known techniques for orbit estimation involve minimum variance Bayesian estimation through either batch processing or Kalman filtering [18]. At their core, both of these algorithms aim to estimate a correction to some a priori state based on minimizing measurement residuals against the a priori state propagated through the nonlinear dynamics. In the case of the batch processor, these corrections are back-propagated to the initial state via a state transition matrix, allowing the processor to converge iteratively; this is helpful because the multiple iterations help overcome the limitations of applying a linear update to the nonlinear dynamics. The Kalman filter, by contrast, produces an update of the state, as well as its associated covariance, after each observation is fused into the estimate. This makes the filter advantageous for estimating quantities that must be continuously updated, such as spacecraft position and velocity. By updating the state after each measurement, there is less need to propagate the state for long periods of time, so the impact of process noise is reduced correspondingly.

Equations 10 and 11 are the crucial components of the Kalman filter. Equation 10 shows that, given the transition matrix $\Phi\left(t_k, t_{k-1}\right)$ between the states at t_{k-1} and t_k, one can compute the a priori covariance P^- at t_k based on the a posteriori covariance P^+ at t_{k-1}. Equation 11 relates the measurement residuals $\tilde{\mathbf{y}}_k$ to the state at time t_k. Based on these two equations, one can compute the Kalman update according to Eqn. 12, where K is the Kalman gain.

$$P_k^- = \Phi\left(t_k, t_{k-1}\right) P_{k-1}^+ \Phi^T\left(t_k, t_{k-1}\right) \tag{10}$$

$$H_k = \frac{\partial \tilde{\mathbf{y}}}{\partial \mathbf{x}} = \begin{bmatrix} \frac{-\rho_y}{\rho_{xy}} & \frac{\rho_x}{\rho_{xy}} & 0 \\ \frac{-\rho_x \rho_z}{\rho_1^2 \rho_{xy}} & \frac{-\rho_y \rho_z}{\rho^2 \rho_{xy}} & \frac{\rho_{xy}}{\rho^2} \end{bmatrix} \tag{11}$$

$$\hat{\mathbf{x}}_k^+ = \hat{\mathbf{x}}_k^- + K_k\left(\tilde{\mathbf{y}}_k - H_k \hat{\mathbf{x}}_k^-\right) \tag{12a}$$

$$P_k^+ = \left(I - K_k H_k\right) P_k^- \tag{12b}$$

B. Synthetic Measurements with Triangulation

Rather than fusing all observations directly, as occurs in the various types of batch processors and Kalman filters, it is sometimes possible to fuse two or more observations together to produce a synthetic observation of some otherwise unobservable quantity, which is then fed into the filter. In some sense, this procedure is used to get the right ascension angle from an equatorial mount; the mount measures local hour angle, which must be fused with an estimate of the local sidereal time in order to get right ascension. In practice, however, the uncertainty in local sidereal time is sufficiently small that the resulting right ascension measurement is treated as a direct observation, rather than a synthetic one.

A notable way this concept can be applied to the optical orbit estimation problem is with triangulation. The most notable limitation on optical sensors is that, being passive sensors, they cannot measure the range to the target. By triangulating the position of an RSO with simultaneous (or near-simultaneous) observations, it is possible to calculate the range of the RSO to either of the ground stations, giving the full position vector of the RSO relative to the ground stations. Conceptually, the algorithm for range computation derives directly from the Law of Sines (Eq. 13), with the geometry depicted in Fig. 2, adapted from [13]. It is important to note that d represents the 3-D distance between the ground stations, not the distance over the surface. While triangulation has been demonstrated with baselines as short as 27 km, for which the difference is negligible, longer baselines are desirable to increase the angular separation between observations and thereby improve accuracy [14]. More typical applications, particularly for objects in higher orbits, involve baselines of hundreds or even thousands of kilometers, for which the **d** vector is appreciably below the surface of the Earth, as is shown in Fig. 2 [19, 20].

$$\frac{\rho_1}{\sin(\theta_2)} = \frac{\rho_2}{\sin(\theta_1)} = \frac{d}{\sin(\gamma)} = \frac{d}{\sin(180^\circ - \alpha - \beta)} \tag{13}$$

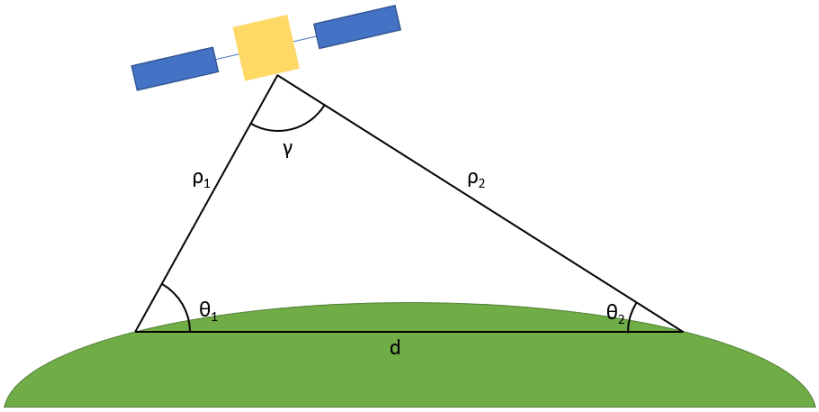

Fig. 2 Geometry for Range Triangulation from Two Ground Stations (adapted from [13])

Consequently, the ranges ρ_1 and ρ_2 can be computed according to Eq. 14

$$\rho_1 = \frac{d \sin(\theta_2)}{\sin(\gamma)} \tag{14a}$$

$$\rho_2 = \frac{d \sin(\theta_1)}{\sin(\gamma)} \tag{14b}$$

However, Eq. 14 assumes that the pointing vectors corresponding to the two observations intersect exactly, which is unlikely to be the case. In addition to sensor pointing errors, the triangulation technique is sensitive to non-simultaneity in the observations [13]. In order to not simply discard information from the second observation vector, we can perform least squares estimation of the satellite's 3-D position; this is possible because the satellite's range and topocentric right ascension and declination from any given ground station uniquely specifies its Cartesian position. Defining the state vector $\mathbf{x}$ as the xyz Cartesian position of the RSO at the time of observation and the observation vector $\tilde{\mathbf{y}}$ according to Eq. 15, we can produce a least-squares estimate $\hat{\mathbf{x}}$ of the satellite's position at each observation epoch according to Eqs. 16 - 18, where $\rho_{xy} = \sqrt{\rho_x^2 + \rho_y^2}$.

$$\tilde{\mathbf{y}} = \begin{bmatrix} \tilde{\alpha}_1 & \tilde{\delta}_1 & \tilde{\alpha}_2 & \tilde{\beta}_2 \end{bmatrix}^T \tag{15}$$

$$W = \text{diag}\left(\begin{bmatrix} 1/\sigma_{\alpha 1}^2 & 1/\sigma_{\delta 1}^2 & 1/\sigma_{\alpha 2}^2 & 1/\sigma_{\delta 2}^2 \end{bmatrix}\right) \tag{16}$$

$$H = \frac{\partial \tilde{\mathbf{y}}}{\partial \mathbf{x}} = \begin{bmatrix} \frac{-\rho_{y1}}{\rho_{xy1}} & \frac{\rho_{x1}}{\rho_{xy1}} & 0 \\ \frac{-\rho_{x1}\rho_{z1}}{\rho_1^2 \rho_{xy1}} & \frac{-\rho_{y1}\rho_{z1}}{\rho_1^2 \rho_{xy1}} & \frac{\rho_{xy1}}{\rho_1^2} \\ \frac{-\rho_{y2}}{\rho_{xy2}} & \frac{\rho_{x2}}{\rho_{xy2}} & 0 \\ \frac{-\rho_{x2}\rho_{z2}}{\rho_2^2 \rho_{xy2}} & \frac{-\rho_{y2}\rho_{z2}}{\rho_2^2 \rho_{xy2}} & \frac{\rho_{xy2}}{\rho_2^2} \end{bmatrix} \tag{17}$$

$$P = \left(H^T W H\right) \tag{18a}$$

$$\hat{\mathbf{x}} = P H^T W \tilde{\mathbf{y}} \tag{18b}$$

This estimate $\hat{\mathbf{x}}$ of the state, having covariance P according to Eq. 18a, can then be fused by the filter. Whether Eq. 14 or Eq. 18 is employed, synthetic position estimates using triangulation have the advantage of fixing the RSO's position at a particular point in time using only observations taken at that time. This makes them especially useful for initial orbit determination [13, 19], but because they provide only three pieces of information rather than the four that the raw observations would provide, this method discards some information compared to putting the observations directly into the filter. It should also be noted that the method of Eqs. 16-18a can be extended to an arbitrary number of ground

stations by adding two additional elements of W and rows of H per ground station. However, in this case, the information discarded is even greater, since directly fusing the observations using a traditional Kalman filter would involve $2n$ observations from n ground stations, versus the three Cartesian position components produced by triangulation.

IV. Assessing Tracking System Performance

Having defined a number of ways to update an estimate of an RSO's orbit, we now focus on analyzing their performance. For the purposes of this work, custody of an RSO at time t is defined as having sufficiently accurate knowledge of an RSO's position then that the object can reliably be observed and distinguished from any other objects that might be nearby. Because of uncertainties in knowledge of the RSO's initial state and the underlying dynamics, the uncertainty in the RSO's propagated state, represented by the covariance, will tend to grow over time. After sufficient time has passed, the locus of possible positions becomes significantly larger than the field of view of the sensors tasked to track it, and it can no longer reliably be found; at this point, custody has been lost. In order to prevent this, regular updates must be made to the state estimate according to one of the procedures in Section III. However, taking the required measurements to perform a state update involves scheduling time on a suitable sensor, which may be limited or costly. It is therefore advantageous to identify which sensors or configurations of sensors can maintain custody of an RSO with a minimum of observation time.

One concern arising in custody maintenance for RSOs is that, when the RSO's state is not well-known, the uncertainty in the RSO's position is not well-modelled by a Cartesian covariance ellipsoid. This is because uncertainty in the vehicle's along-track position in the orbital plane typically greatly exceeds the uncertainties in radial or cross-track direction. Moreover, while the dynamics of the problem, particularly the conservation of angular momentum, keep the uncertainties in the radial and cross-track components bounded, the uncertainty in the along-track direction will grow without bound. Over time, this creates a "banana-shaped" distribution of orbital positions, and, in the extreme case, a toroidal distribution, representing a relatively well-known orbital plane but very little knowledge of the RSO's position along the orbital path [21]. This heterogeneous growth in the position covariance matrix is shown in Fig. 3, which shows the diagonal elements of the position covariance matrix in the BVH frame, where the V direction is along the spacecraft's velocity vector, the H direction is along the angular momentum vector, and the B direction completes the right handed set. As can be seen in the figure, the position standard deviation in the B and H directions, normal to the direction of motion, remain relatively small, while the V component grows more or less linearly with time.

Figure 3 also provides some insight into how to analyze the performance of a tracking system. Since the position uncertainty of the RSO, represented by the position covariance, will grow without bound in the absence of measurement updates, the rate at which it does so is a key measure of tracking system performance. More effective tracking systems will maintain better position solutions for longer periods of time, reducing the frequency of the required measurement updates. To reduce the 3x3 position covariance matrix (which is itself a subset of the 6x6 state covariance matrix) to a

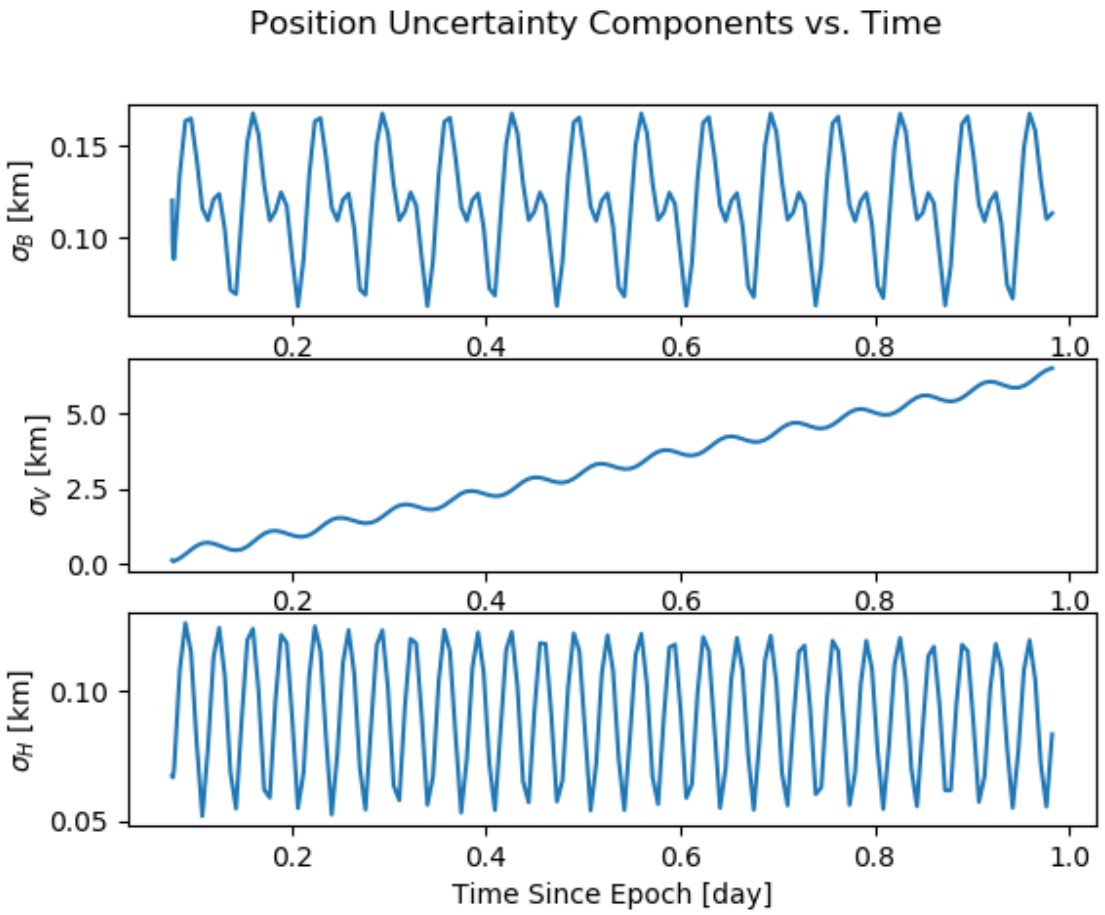

Fig. 3 Position Uncertainty Components vs. Time

scalar value, we take the square root of the trace of the position covariance, denoted by σ_p; this represents the 3-D position uncertainty in the RMS sense, with units of kilometers. While the evolution of σ_p over time can be used directly to quantify tracking system performance, the angular RSO's position uncertainty σ_θ (given by Eqn. 19, where h is the altitude of the RSO) when viewed from the ground is more directly relevant in evaluating custody of the RSO; a 20 km position error may be fatal to efforts to find the object in LEO, while in GEO this would be only about 2 arcmin, well within the field of view of most tracking telescopes [7–9]. To this end, a key figure of merit used to assess tracking system performance in Section V is the time it takes for a system to violate some σ_θ bound after the last measurement epoch.

$$\sigma_\theta = \arctan\left(\frac{\sigma_p}{h}\right) \tag{19}$$

In order to analyze the effect of tracking station distribution on tracking accuracy, it is also necessary to define a measure of the distribution of the tracking stations. For a two-station network, a natural measurement would be the

distance between the ground stations and the compass bearing from one to the other, but this suffers from at least two problems. First, there is no clear way to generalize it to a network of more than two ground stations. Second, and perhaps more importantly, it is dependent on the orbital regime under consideration. For example, while a 200 km baseline may provide diversity of observational geometry for an object in LEO, it provides basically the same view of an object in GEO. We thus introduce the concept of observational geometric diversity GD_o, which quantifies the spread of the ground station line of site vectors when viewed from the RSO. GD_o is defined on a scale from 0 to 100, with 0 representing identical look directions and 100 representing the greatest possible spread between look directions. For two ground stations, GD_o simply proportional to the angle θ_o between the vectors from the RSO to the ground station (Eqn. 20a); full geometric diversity is defined as the stations being in opposite directions when viewed from the RSO. For systems with more than two ground stations, the RSO-ground station vectors are extended to the unit sphere centered on the RSO, and the smallest convex spherical polygon that encloses all of the RSO-ground station vectors is computed. The GD_o in this case is proportional to the solid angle Ω_o subtended by this spherical polygon (Eqn. 20b), and full geometric diversity is achieved when this spherical polygon is a hemisphere (the case of observers behind the RSO in space is not considered).

$$GD_o = 100\frac{\theta_o}{\pi} \tag{20a}$$

$$GD_o = 100\frac{\Omega_o}{2\pi} \tag{20b}$$

To help illustrate this concept, Fig. 4 shows the evolution of GD_o vs. time for the observation geometries shown in Fig. 5. As the RSO first comes into view of the ground stations, the distances between them are small in comparison to the slant ranges to the RSO, so the look directions are close together, for a low value of GD_o. This is the situation depicted in Fig. 5 (b) and (d) for $n = 3$ and 4 ground stations, respectively. As the RSO gets closer, the look directions spread out, so GD_o increases; Figs. 5 (a) and (c) show the instant where GD_o is maximized in each case. For $n = 3$, the solid angle subtended by the the look directions at this time is 0.465 steradians, or 7.4% of 2π, so $GD_o = 7.4$; for $n = 4$, the solid angle is 0.793 steradians, or 12.6% of 2π, so $GD_o = 12.6$. After the RSO passes by the ground stations and the slant range increases, the look directions again move closer together, and GD_o decreases, consistent with the symmetry of Fig. 4.

Observational geometric diversity has several desirable properties. First, it is consistent with the intuitive notion of baseline distance; more spread out ground stations will increase GD_0. Second, it penalizes redundant observations by taking the convex hull of ground station locations; adding a ground station that is between other, existing ground stations will not increase GD_0. Finally, because it is based on the angular distances between ground stations rather than linear distances, it naturally accommodates RSOs at different orbital altitudes.

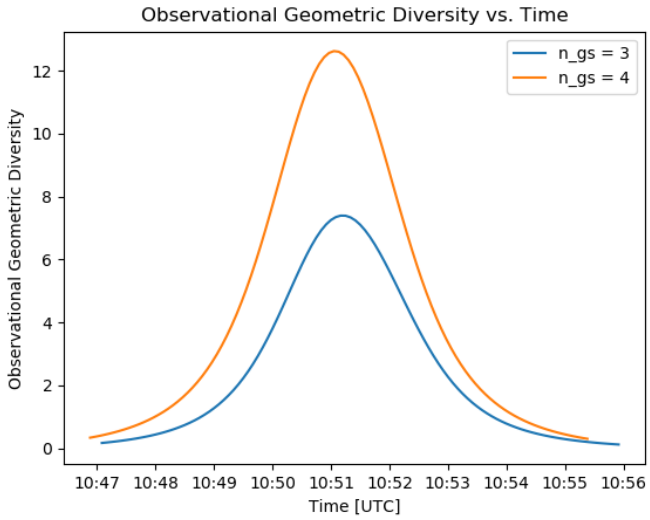

Fig. 4 GD_o **vs. Time**

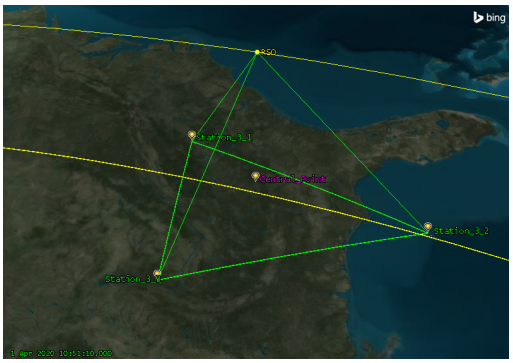

(a) $n = 3$**, maximum** GD_o

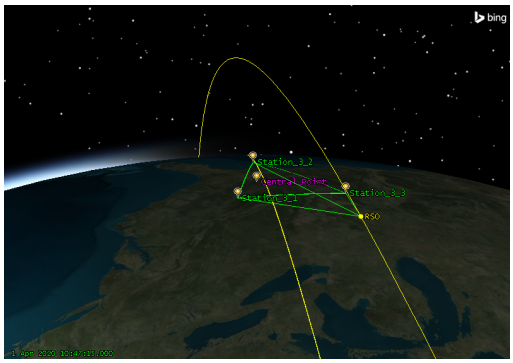

(b) $n = 3$**, low** GD_o

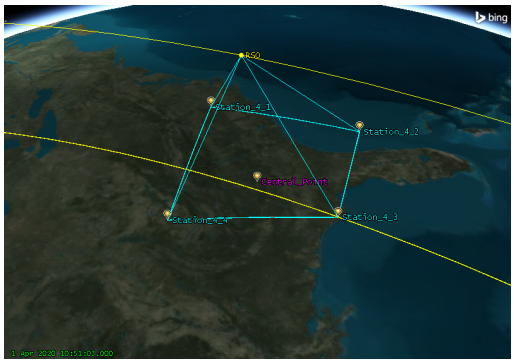

(c) $n = 4$**, maximum** GD_o

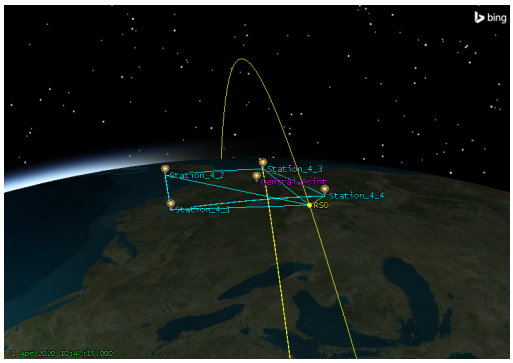

(d) $n = 4$**, low** GD_o

Fig. 5 Satellite Observation Geometry

V. Simulation Setup

In order to evaluate the performance of various sensor configurations with the different orbital estimation strategies, we used the Jet Propulsion Laboratory's Mission Analysis, Operations, and Navigation Toolkit Environment (MONTE)

Orbit	Periapsis altitude (km)	Apoapsis Altitude (km)	Inclination (deg)	Arg. of Periapsis (deg)
LEO	500	600	98.2	0
MEO	20178	20184	54.9	0
GTO	250.4	35786	35	0
GEO	35786	35786	0.001	0

Table 1 RSO Initial States

	Position			Velocity		
Orbit	σ_B (km)	σ_V (km)	σ_H (km)	σ_B (m/s)	σ_V (m/s)	σ_H (m/s)
LEO	0.1	10	0.1	0.5	0.5	0.5
MEO	1	25	1	0.5	0.5	0.5
GTO	1	50	1	0.5	0.5	0.5
GEO	1	50	1	0.5	0.5	0.5

Table 2 RSO Initial State Uncertainties

orbital mechanics software to perform a series of Monte Carlo simulations for a variety of different orbits [22]. For each of the orbits described in Table 1, 500 Monte Carlo iterations were performed for each of $n = 1, 2, \ldots 5$ ground stations for the Kalman filtering strategy described in Section III (A) and each of $n = 1, 2, \ldots, 4$ ground stations for the triangulation strategy of Section III (B), for a total of 4500 Monte Carlo runs for each orbit. For each Monte Carlo run, the initial state of the spacecraft was randomly perturbed using the uncertainties in Table 2, and the ground stations were randomly distributed about a central point using the parameters in Table 3; these minimum and maximum distances from the central point were selected to guarantee reasonably large separation between the ground stations while ensuring all ground stations would be able to view the RSO simultaneously. The ground stations were distributed within the region of interest uniformly with respect to area, subject to the constraint that the bearings from the central point to adjacent ground stations had to be separated by at least $720/3n$ degrees (i.e., at least two-thirds of the spacing obtained by distributing the bearings evenly around a circle). The central point for the ground stations was selected such that the RSO was visible from the central point within a few hours after the simulation epoch, and, for the LEO and MEO cases, the RSO passes over the central point at an elevation angle of at least 85°. Typical observation geometries for the LEO case for $n = 3$ and 4 ground stations are presented in Fig. 5; note how the ground stations are distributed relatively evenly around the central point, rather than being clustered off to one side. This is a consequence of the angular separation constraint; a uniformly random distribution of locations would lead to many cases where the ground stations are tightly packed together, severely limiting the achievable values of GD_o. The other orbit cases have similar ground station configurations, with the distances from the central point modified according to Table 3.

In each Monte Carlo run, each ground station observed the RSO on the first pass it made over the ground station; the simulation epoch was selected such that this pass occurred when the ground stations were in darkness and the RSO was

Orbit	Min. GS Distance from Center (km)	Max. GS Distance from Center (km)	Max. σ_θ (deg.)
LEO	100	600	0.5
MEO	300	1000	0.2
GTO	500	2000	0.2
GEO	500	2000	0.2

Table 3 Ground Station Parameters

illuminated. If RSO was visible to the ground station for more than half an hour, the observation duration was limited to the half hour at the center of the access window in order to simulate sensor tasking constraints that would require a ground station to observe multiple targets per night. Each ground station made simulated right ascension-declination observations of the RSO at 5 s intervals, and zero-mean Gaussian noise with $\sigma = 1$ arcmin was added to each of the right ascension and declination measurements in order to simulate the measurement noise of the sensor. The observations were fed into a Kalman filter, either directly or via triangulation, in order to estimate the RSO's state, and the resulting covariance was propagated for 48 h after the last observation was made. For each run, the maximum values of σ_p and GD_o were recorded, as was the time it took the σ_θ limits in Table 3 to be violated after the end of the observation window; these limits were selected as being similar to the fields of view of sensors that might be tasked to track an object in these orbital regimes [7–9, 14, 23].

VI. Results

A. Comparison of Orbit Determination Algorithms and Effect of Multiple Ground Stations

Figures 6 through 13 show the performance of the tracking systems over the various orbital regimes considered. Figures 6, 8, 10, and 12 summarize the time between the last observation and violation of the σ_θ bound from Table 3 for the median, 10th percentile, and 90th percentile of Monte Carlo runs for each configuration. Figures 7, 9, 11, and 13 show all Monte Carlo runs, and present σ_θ violation time versus the amount of time between the first and last observations of all the ground stations.

Before comparing the performance of the different orbital estimation strategies, a few features on these charts merits discussion. First, the distribution of σ_θ violation times in several cases is strongly multimodal. This is a consequence of the periodic behavior of the position covariance, shown in Figure 3. Long-term growth in σ_p is roughly linear, but it displays short-term periodic behavior corresponding to the spacecraft's motion around the orbit. Thus, the time it takes for σ_p, and thus σ_θ, to exceed some fixed value can be shifted by one (or potentially more) orbital periods in either direction by sufficiently large changes to the phase of the periodic terms. This behavior is seen in the LEO case (Figure 7), which shows four distinct groupings; the spacing between each group matches the 1.6 h orbital period. This behavior is also seen, to a much lesser degree, in the MEO case, where the two groups are separated by about 40% of the 12 h

orbital period. Another artifact is the distribution of observation lengths; because each ground station was constrained to observe the RSO for no more than 30 minutes to simulate operational sensor tasking constraints, and the triangulation method requires simultaneous observations of the RSO, many of the triangulation cases have the same total observation duration of 30 minutes. The cases without triangulation are less constrained by this, since the RSO generally comes into view of different stations at different times, so tracking can be continuously maintained for longer periods of time. It is also worth noting that GTO was the only case in which σ_θ violation time was consistently less than the orbital period. GTO was also the only case with significant eccentricity, which makes the dynamics more nonlinear; it is possible that this disparity would be improved by using an extended or unscented Kalman filter, which are better suited to nonlinear problems than the linear filter used here.

Comparing the summary figures (Figs. 6, 8, 10, and 12), it is difficult to identify either estimation scheme as superior across all orbital regimes. While the Kalman filter without triangulation clearly outperformed the triangulation scheme in LEO and was generally superior in MEO, the triangulation method measurably outperformed the no-triangulation method in GTO. In GEO, the no-triangulation scheme had better performance for $n = 2$ ground stations, but triangulation performed better for $n = 3, 4, 5$, though only for $n = 5$ was there clear separation between the two methods. In almost all cases, increasing the number of ground stations was correlated with better performance. However, it must be noted that these differences are not especially large in absolute terms. Except for the $n = 1$ case in GEO, the largest spread between the 10th percentile of the worst case and the 90th percentile of the best case was 0.9 h in MEO (vs. a nominal value of approximately 14 h), 1.4 h in GTO (vs. 7 h nominal), and 3.4 h in GEO (vs. 30 h nominal). These statistics are less meaningful for LEO, where the distribution is strongly multimodal, but the largest difference is 3.2 h against a nominal value of 15 h for the largest cluster of data points. Again, with the exception of $n = 1$ for GEO, the improvement between the 10th percentile worst case and 90th percentile best case is 24% for LEO, 6% for MEO, 20% for GTO, and 12% for GEO. Whether or not these differences are operationally significant will necessarily depend on specific tracking requirements and available resources, but if the observations are available, using them will provide some benefit.

The significant exception to this trend is the large difference between $n = 1$ and $n = 2$ in GEO. Median performance for $n = 1$ is 19.7 h vs. 30.0 h for $n = 2$ with triangulation or 13.2 h without, an increase of 50%. Critically, this takes the revisit period from significantly less than a day to more than a day, allowing for the same set of sensors to observe the object nightly without violating the angular uncertainty limit. As noted above, though, the benefits of moving beyond two ground stations are much more modest.

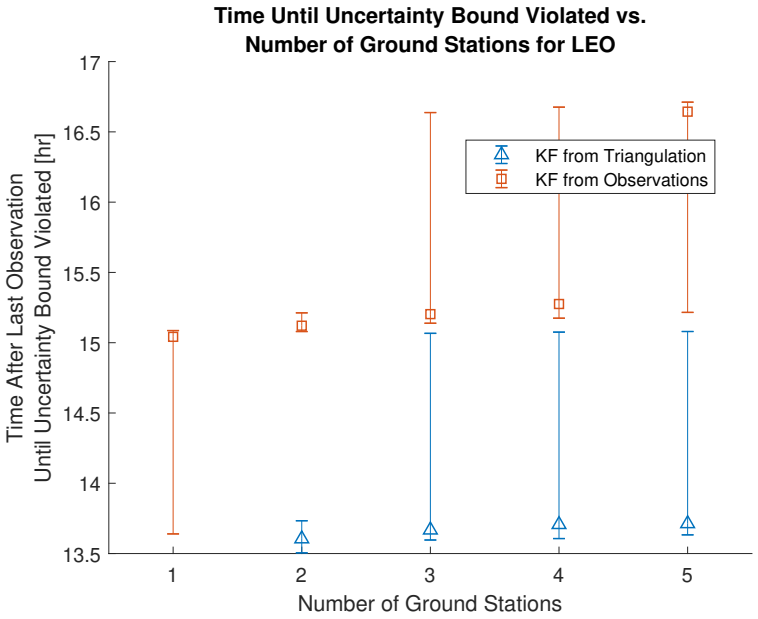

Fig. 6 Time Until σ_θ Bound Violated vs. Number of Ground Stations for LEO

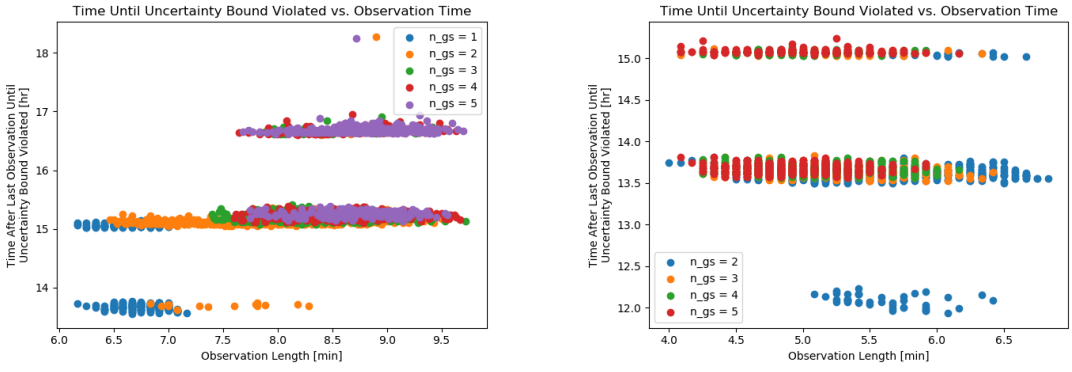

(a) Without Triangulation **(b) With Triangulation**

Fig. 7 Time Until σ_θ Bound Violated vs. Total Observation Time for LEO

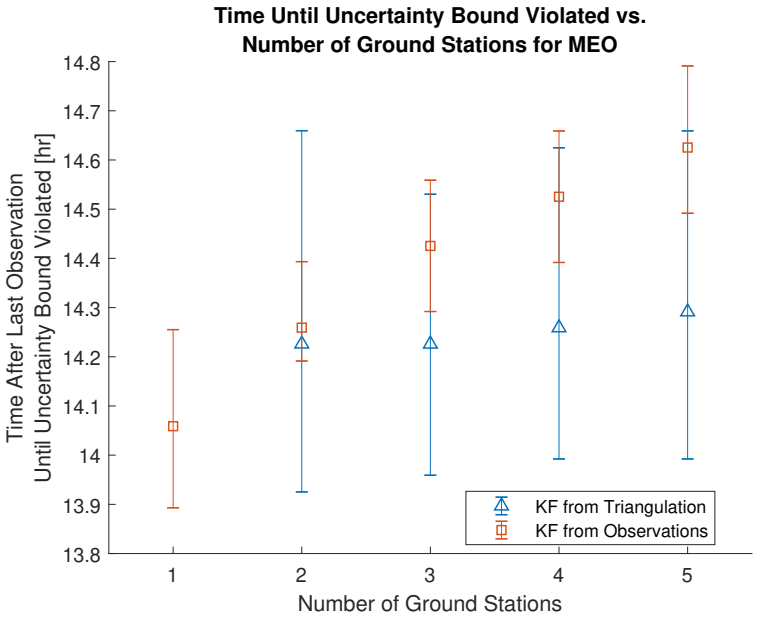

Fig. 8 Time Until σ_θ Bound Violated vs. Number of Ground Stations for MEO

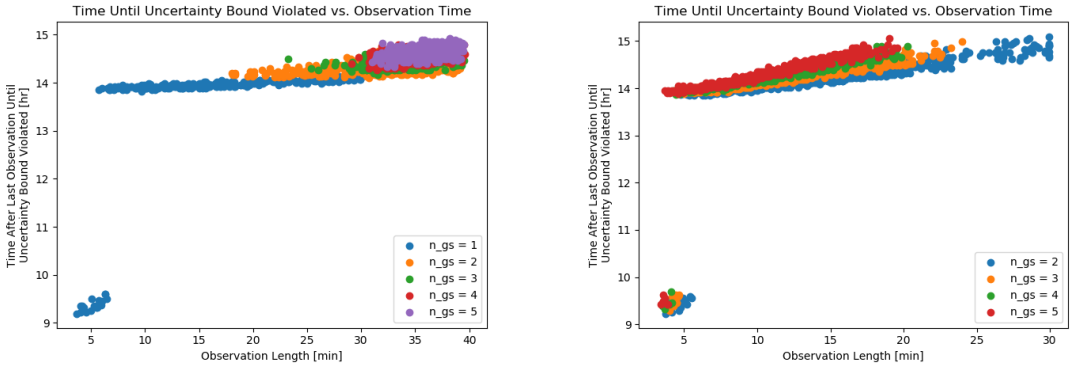

(a) Without Triangulation **(b) With Triangulation**

Fig. 9 Time Until σ_θ Bound Violated vs. Total Observation Time for MEO

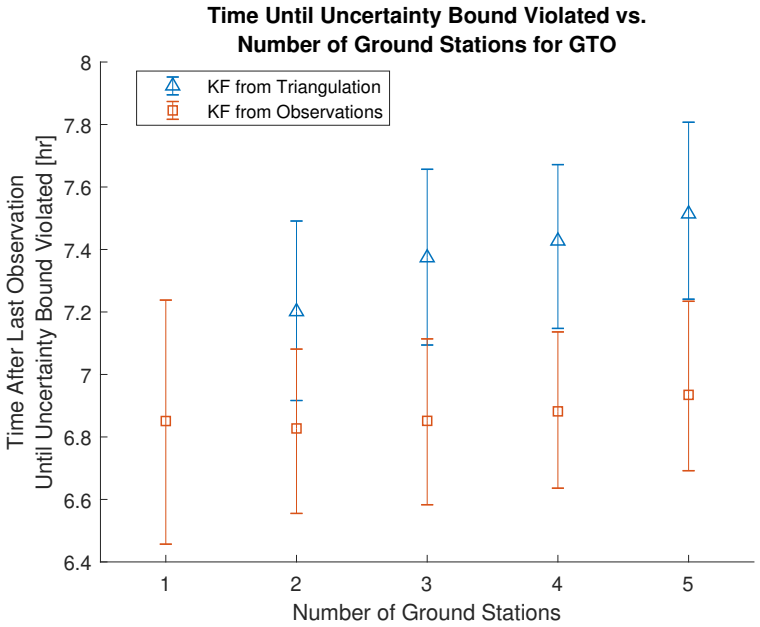

Fig. 10 Time Until σ_θ Bound Violated vs. Number of Ground Stations for GTO

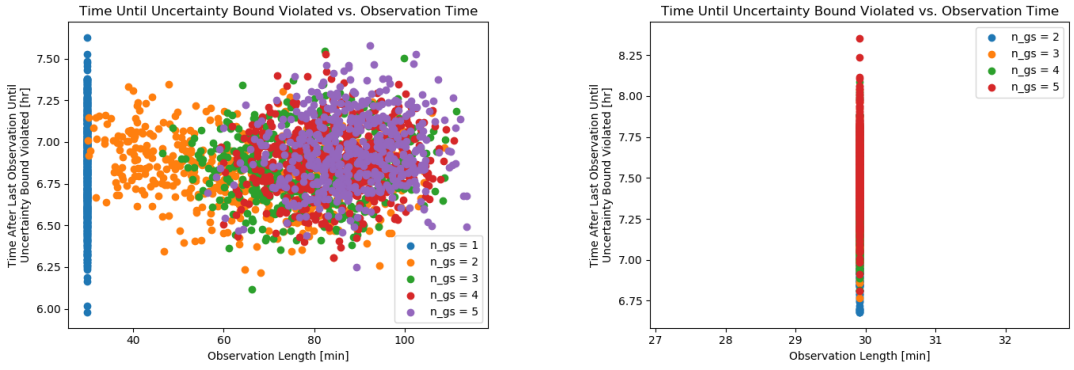

(a) Without Triangulation **(b) With Triangulation**

Fig. 11 Time Until σ_θ Bound Violated vs. Total Observation Time for GTO

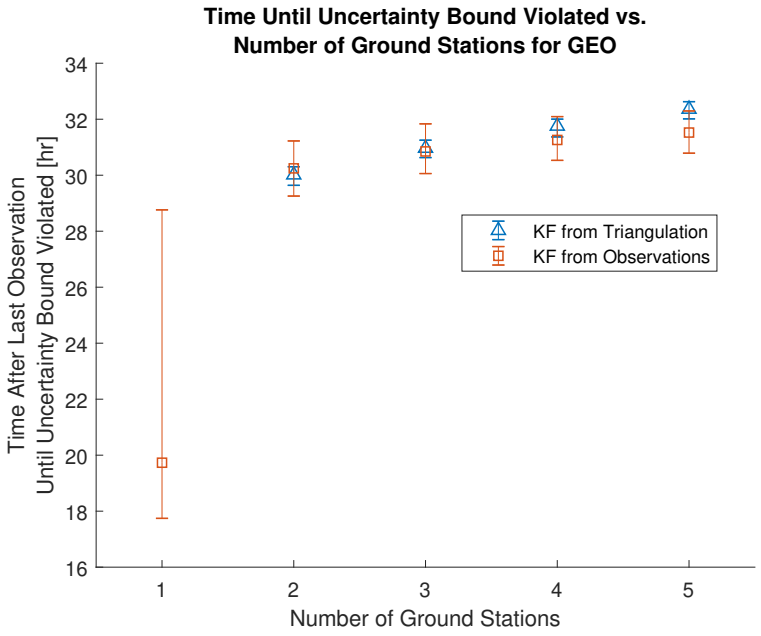

Fig. 12 Time Until σ_θ Bound Violated vs. Number of Ground Stations for GEO

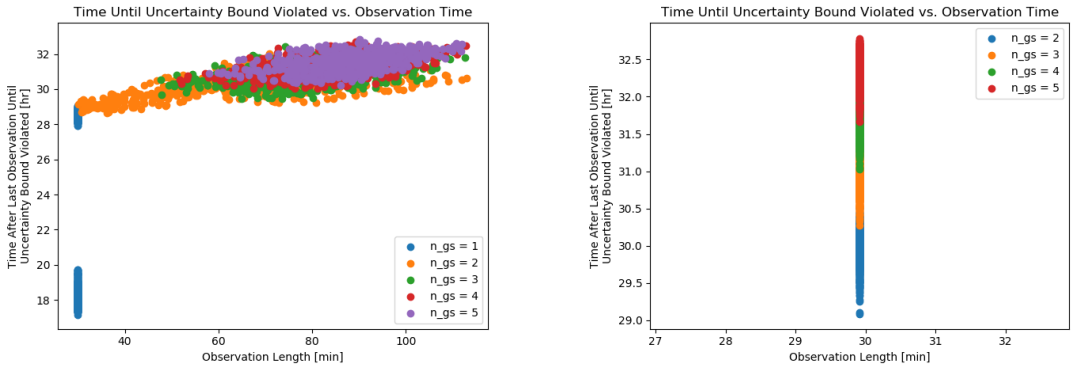

(a) Without Triangulation **(b) With Triangulation**

Fig. 13 Time Until σ_θ Bound Violated vs. Total Observation Time for GEO

B. Effects of Ground Station Location

Having examined the effects of different numbers of tracking stations n and the fusion algorithm used, we now investigate the impact of the location of the various sensors for a particular n. Figures 14-21 present the time it takes for the σ_θ bound to be violated after the last observation as a function of the maximum observational geometric diversity GD_0 achieved on each Monte Carlo run. As noted above, the differences between the best- and worst- performing cases is often not large in absolute terms; nevertheless, some sensor configurations show a clear trend of more spread out ground stations leading to better orbit solutions. This is most clearly seen with the MEO without triangulation (Fig. 16) and GTO with triangulation cases (19,) where there is a clear positive correlation between GD_0 and σ_θ violation times, and R^2 values on the regression are consistently higher than 0.30, and as high as 0.69. Notably, these cases also have some of the smallest spreads between best- and worst-performing Monte Carlo runs. The GEO cases (Figs. 20 and 21) also show a correlation, though the R^2 values are smaller. Both LEO cases are strongly multimodal, and the MEO with triangulation case is also somewhat multimodal; the performance of a ground station configuration based on σ_θ violation time in these cases is going to be dictated by which peak of the distribution the case falls into, which in most case does not seem to be well-correlated with GD_0.

One other question that must be addressed when evaluating the effect of GD_0 is whether it is merely a proxy for total observation time; a ground station network that is more spread out will tend to acquire an RSO sooner and loose sight of it later, and this temporal diversity in observations may be useful in ways that geometric diversity is not, particularly for inferring velocity information. Figures 7, 9, 11, and 13 show σ_θ violation time vs total observation time (time between the first and last observations, regardless of ground station), and in both MEO cases (Fig. 9) and the GEO without triangulation case (Fig. 13a), there is a clear positive correlation between total observation time and σ_θ violation time. However, for both the GTO and GEO with triangulation cases (Figs. 11b and 13b) the requirement of simultaneous observations for triangulation and the imposed 30 min limit on maximum observation duration per ground station mean that the total observation time is the same for all cases. Since both of these cases showed reasonably strong correlations between GD_0 and σ_θ violation time ($R^2 > 0.36$ in GTO and 0.12 in GEO), there is some evidence that spreading out the ground stations does provide some benefit in terms of the quality of the orbit solution, even in the absence of improved total observation durations.

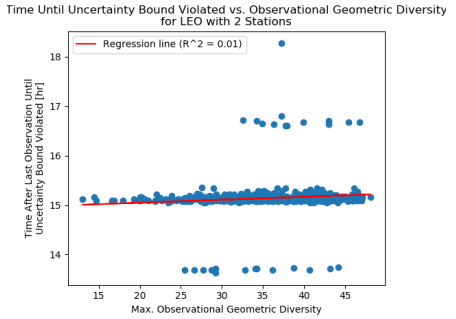

(a) n=2

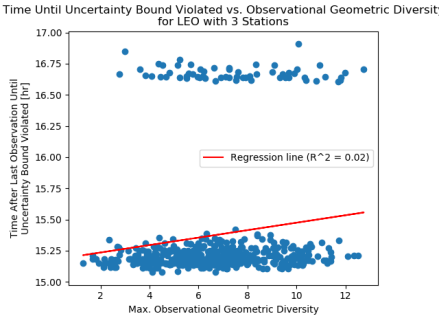

(b) n=3

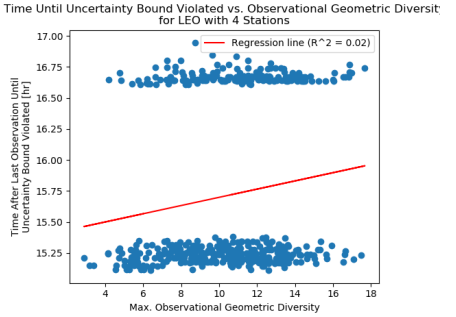

(c) n=4

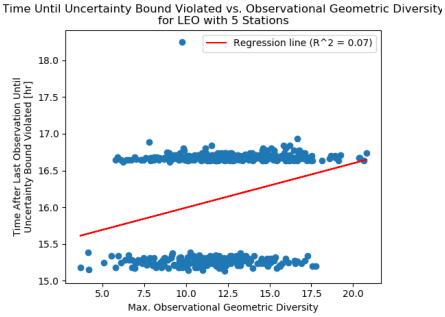

(d) n=5

Fig. 14 Time Until σ_θ Bound Violated vs. GD_O for LEO, Kalman Filter Case

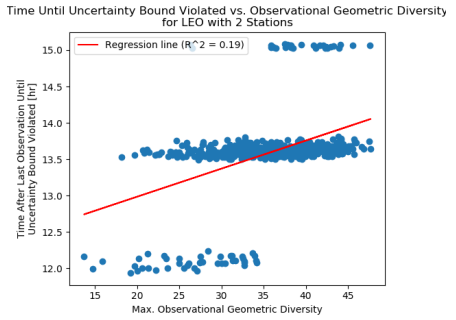

(a) n=2

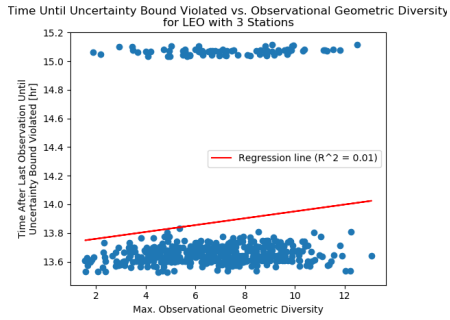

(b) n=3

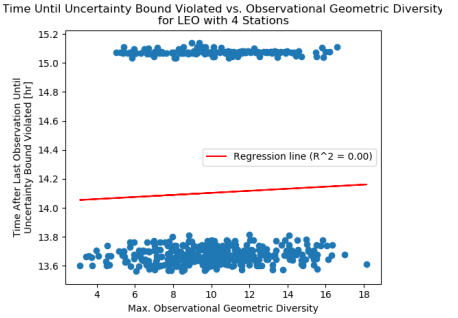

(c) n=4

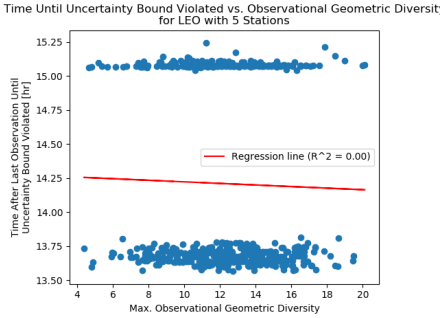

(d) n=5

Fig. 15 Time Until σ_θ Bound Violated vs. GD_O for LEO, Triangulation Case

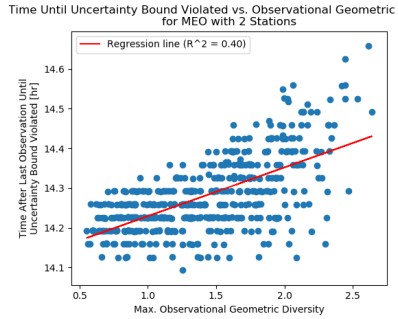

(a) n=2

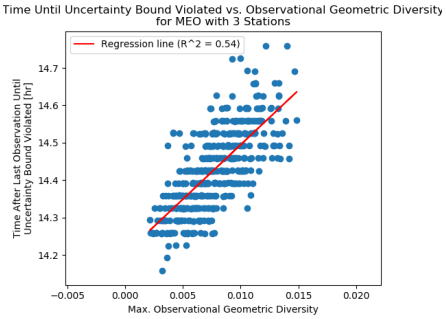

(b) n=3

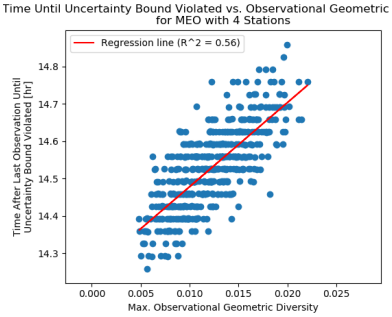

(c) n=4

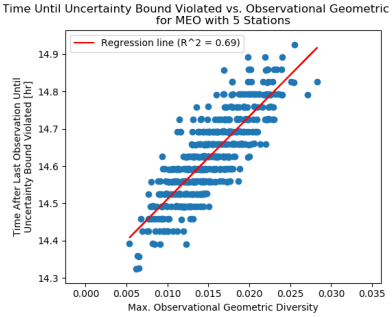

(d) n=5

Fig. 16 Time Until σ_θ Bound Violated vs. GD_O for MEO, Kalman Filter Case

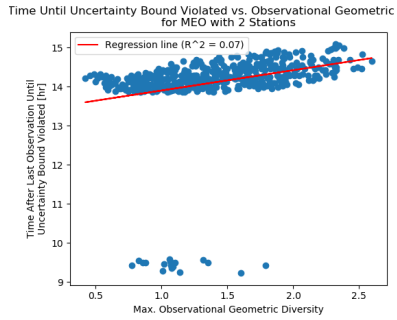

(a) n=2

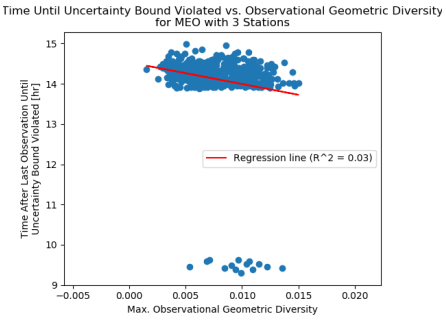

(b) n=3

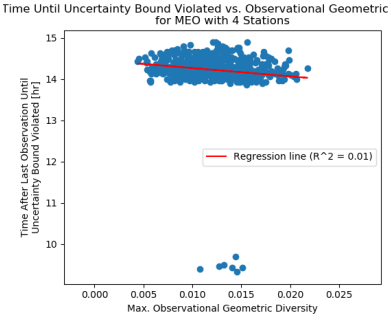

(c) n=4

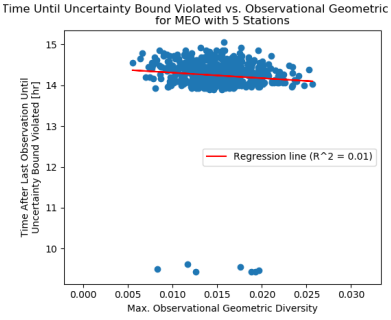

(d) n=5

Fig. 17 Time Until σ_θ Bound Violated vs. GD_O for MEO, Triangulation Case

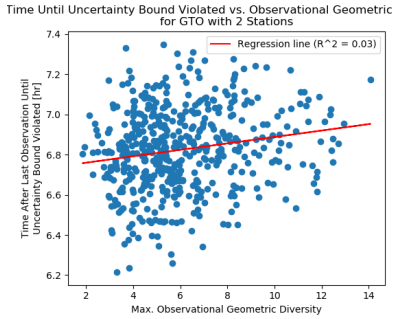

(a) n=2

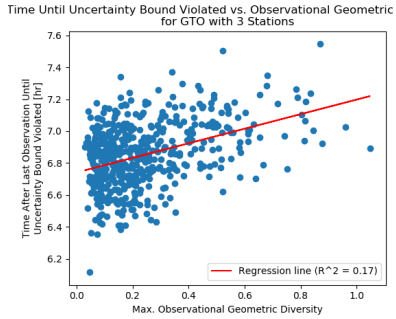

(b) n=3

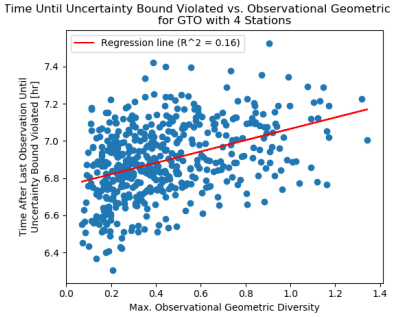

(c) n=4

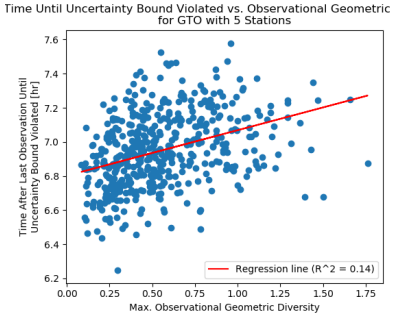

(d) n=5

Fig. 18 Time Until σ_θ Bound Violated vs. GD_O for GTO, Kalman Filter Case

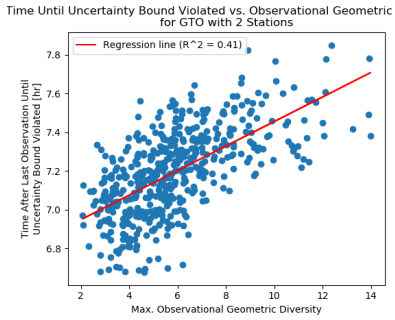

(a) n=2

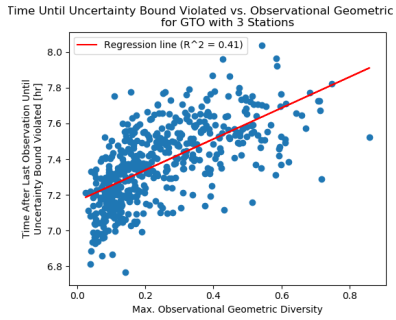

(b) n=3

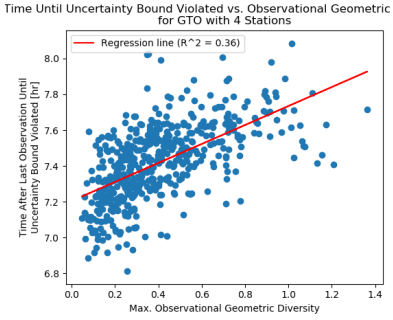

(c) n=4

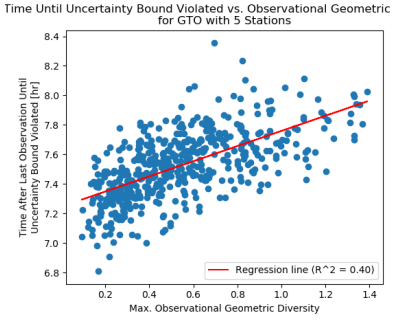

(d) n=5

Fig. 19 Time Until σ_θ Bound Violated vs. GD_O for GTO, Triangulation Case

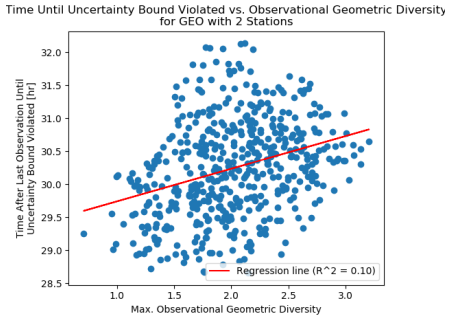

(a) n=2

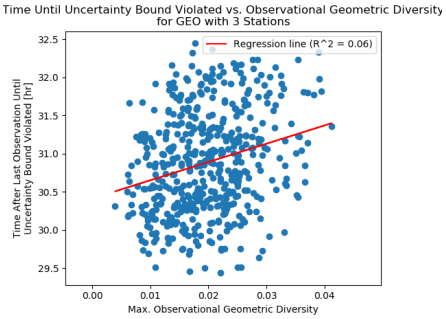

(b) n=3

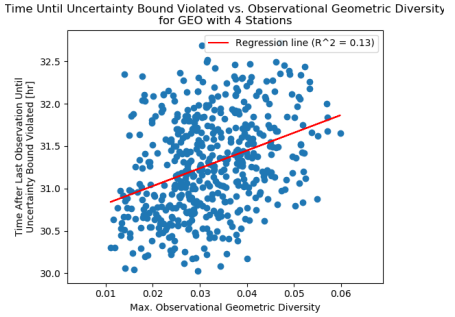

(c) n=4

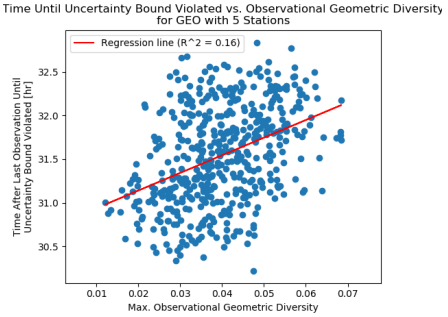

(d) n=5

Fig. 20 Time Until σ_θ Bound Violated vs. GD_O for GEO, Kalman Filter Case

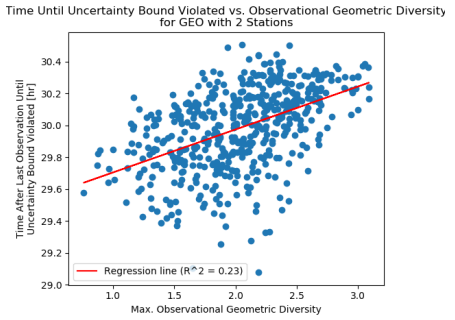

(a) n=2

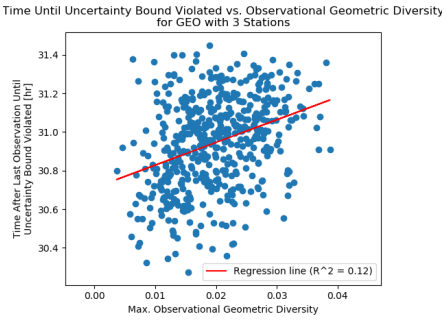

(b) n=3

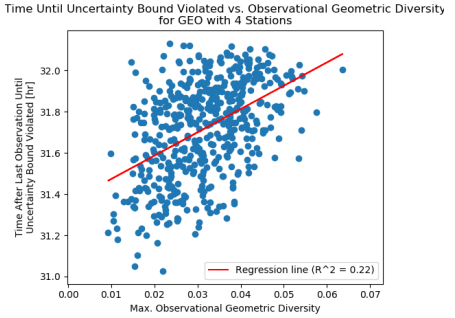

(c) n=4

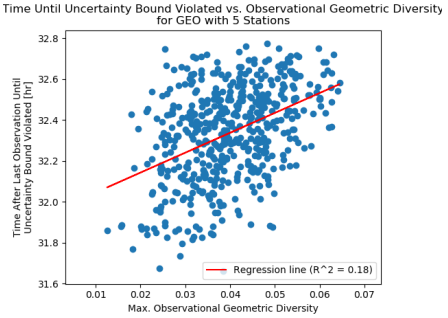

(d) n=5

Fig. 21 Time Until σ_θ Bound Violated vs. GD_O for GEO, Triangulation Case

VII. Conclusion

In this work, we have assessed different strategies for using geographically dispersed optical sensors to maintain custody of RSOs in various orbital regimes. We used 18,000 Monte Carlo runs of different ground station configurations, orbits, and tracking algorithms to compare a traditional Kalman filtering strategy against an algorithm that uses simultaneous observations from multiple ground stations at each observation epoch to triangulate the RSO's position. We considered objects in LEO, MEO, GTO, and GEO and networks of up to 5 ground stations, with each ground station being no more than 2000 km from a central point along the orbit's path. Performance in each case was assessed based on how long the tracking system could maintain custody of the RSO after taking the last observation, and loss of custody was determined by the uncertainty of the RSO's position when viewed from the ground.

We established that triangulation based on simultaneous observations from multiple ground stations is a credible tracking strategy, insofar as it performs comparably to more traditional Kalman filtering strategies; however, neither strategy demonstrated consistently better performance in call cases. Across the different orbital regimes, the differences in performance between the 10th percentile worst case and 90th percentile best case ranged from 6% to 24%, so selecting the most advantageous strategy for the particular RSO of interest can appreciably increase tracking system performance. We also showed that dispersing ground stations farther away from each other in many cases resulted in modest (3% - 10%) improvements in system performance in many cases.

One area in which the present analysis could be refined is in applying more sophisticated filtering algorithms. The present work used a traditional (i.e., linear) Kalman filter in both cases; even in the triangulation case, a Kalman filter was used to propagate the RSO's state between measurement epochs. While an attempt was made to use operationally realistic uncertainty inputs, a thorough sensitivity and tuning analysis of the filter was not performed, which could be beneficial. Moreover, using a linear filter for a nonlinear problem like orbit estimation increases the risk of filter divergence, and linear covariance propagation will break down if covariance growth becomes too large [21]. While the particular cases in this analysis were selected to avoid the worst of these problems, applying more sophisticated techniques like extended or unscented Kalman filters could improve performance, particularly in GTO, where the dynamics are especially difficult due to the eccentric nature of the orbit.

While this analysis focused on ground station networks capable of taking simultaneous observations, whether or not they were so employed, another logical extension would be to examine networks of ground stations dispersed on intercontinental scales. Such networks trade increased accuracy at the observation epoch for more frequent measurement updates. Given the inevitable nature of along-track covariance growth (Fig. 3), such strategies may achieve better results for the same total amount of sensor time.

A final area for future work is exploring the tradeoffs between designing tracking station networks for particular orbital regimes. While the present work considered specific orbit cases individually and selected tracking network parameters suitable for each, a real-life network will likely be interested in tracking many objects in diverse orbital

regimes, though some (e.g., GEO) may be higher priority than others. Optimizing the network for one particular case seems likely to be detrimental to performance in other cases, and an exploration of these tradeoffs would complement the present work by analyzing more operationally realistic scenarios.

Acknowledgments

Research assistantship funding for Luke Renegar was provided by Georgia Tech Research Institute's Independent Research and Development (IRAD) program. The authors gratefully acknowledge the Jet Propulsion Laboratory for providing access to their MONTE orbital mechanics toolkit, and Analytical Graphics, Inc. for making the Systems Toolkit (STK) software publicly available free of charge.

References

[1] Chatters, E. P., and Crothers, B. J., "Space Surveillance Network," *Space Primer*, Air University Press, Maxwell Air Force Base, Alabama, 2009, 3rd ed., pp. 249–258.

[2] Kahr, E., Montenbruck, O., and O'Keefe, K. P. G., "Estimation and Analysis of Two-Line Elements for Small Satellites," *Journal of Spacecraft and Rockets*, Vol. 50, No. 2, 2013, pp. 433–439. https://doi.org/10.2514/1.A32352.

[3] Psiaki, M. L., "Gaussian-Mixture Kalman Filter for Orbit Determination Using Angles-Only Data," *Journal of Guidance, Control, and Dynamics*, Vol. 40, No. 9, 2017, pp. 2341–2347. https://doi.org/10.2514/1.G002812.

[4] Früh, C., and Schildknecht, T., "Accuracy of Two-Line-Element Data for Geostationary and High-Eccentricity Orbits," *Journal of Guidance, Control, and Dynamics*, Vol. 35, No. 5, 2012, pp. 1483–1491. https://doi.org/10.2514/1.55843.

[5] Shuster, S. P., "A Survey and Performance Analysis of Orbit Propagators for LEO, GEO, and Highly Elliptical Orbits," Master's thesis, Utah State University, Logan, Utah, 2017.

[6] Pearlman, M. R., Degnan, J. J., and Bosworth, J. M., "The International Laser Ranging Service," *Advances in Space Research*, Vol. 30, No. 2, 2002, pp. 135 – 143. https://doi.org/https://doi.org/10.1016/S0273-1177(02)00277-6.

[7] Park, J.-H., Yim, H.-S., Choi, Y.-J., Jo, J. H., Moon, H.-K., Park, Y.-S., Bae, Y.-H., Park, S.-Y., Roh, D.-G., Cho, S., Choi, E.-J., Kim, M.-J., and Choi, J., "OWL-Net: A Global Network of Robotic Telescopes for Satellite Observation," *Advances in Space Research*, Vol. 62, No. 1, 2018, pp. 152–163. https://doi.org/10.1016/j.asr.2018.04.008.

[8] Chun, F. K., Tippets, R. D., Dearborn, M. E., Gresham, K. C., Freckleton, R. E., and Douglas, M. W., "The U.S. Air Force Academy Falcon Telescope Network," *Proceedings of the 2014 Advanced Maui Optical and Space Surveillance Technologies Conference*, Maui, 2014.

[9] Coder, R. D., Jaunzemis, A. D., Mathew, M. V., Worthy, J. L., and Holzinger, M. J., "Georgia Tech Space Object Research Telescope," *Journal of Spacecraft and Rockets*, Vol. 54, No. 6, 2017, pp. 1399–1403. https://doi.org/10.2514/1.A33852.

[10] Vallado, D. A., and McClain, W. D., *Fundamentals of Astrodynamics and Applications*, 4th ed., Microcosm Press, Hawthorne, CA, 2013.

[11] Schaeperkoetter, A. V., "A Comprehensive Comparison Between Angles-Only Initial Orbit Determination Techniques," Master's thesis, Texas A&M University, College Station, TX, Dec. 2011.

[12] Der, G. J., "New Angles-only Algorithms for Initial Orbit Determination," *Proceedings of the 2012 Advanced Maui Optical and Space Surveillance Technologies Conference*, Maui, 2012.

[13] Bernard, A. J., Nafi, A. M., and Geller, D. K., "Using Triangulation in Optical Orbit Determination," *Proceedings of the 2018 AAS/AIAA Astrodynamics Specialist Conference*, Advances in the Astronautical Sciences, Vol. 167, Univelt, Escondido, CA, 2018, pp. 2903–2916.

[14] Zimmer, P., McGraw, J. T., and Ackermann, M. R., "Real-Time Surveillance of LEO and MEO with Small Optical Telescopes," *Proceedings of the 2015 Advanced Maui Optical and Space Surveillance Technologies Conference*, Maui, 2015.

[15] DeMars, K. J., McCabe, J. S., and Darling, J. E., "Collaborative and Multi-Sensor Tracking and Data Fusion," *Spaceflight Mechanics 2015*, Advances in the Astronautical Sciences Series, Vol. 155, Univelt, Escondido, CA, 2015, pp. 583–602.

[16] Lang, D., Hogg, D. W., Mierle, K., Blanton, M., and Roweis, S., "Astrometry.net: Blind Astrometric Calibration of Arbitrary Astronomical Images," *The Astronomical Journal*, Vol. 139, No. 5, 2010, pp. 1782–1800. https://doi.org/10.1088/0004-6256/139/5/1782.

[17] Spratling, B., and Mortari, D., "A Survey on Star Identification Algorithms," *Algorithms*, Vol. 2, No. 1, 2009, pp. 93–107. https://doi.org/10.3390/a2010093.

[18] Tapley, B. D., Schutz, B. E., and Born, G. H., *Statistical Orbit Determination*, Elsevier Academic Press, Amsterdam, 2004.

[19] Porfilio, M., Piergentili, F., and Graziani, F., "Two-site Orbit Determination: The 2003 GEO Observation Campaign from Collepardo and Mallorca," *Advances in Space Research*, Vol. 38, No. 9, 2006, pp. 2084–2092. https://doi.org/10.1016/j.asr.2006.06.004.

[20] Choi, J., Choi, Y.-J., Yim, H.-S., Jo, J.-H., and Han, W.-Y., "Two-Site Optical Observation and Initial Orbit Determination for Geostationary Earth Orbit Satellites," *Journal of Astronomy and Space Sciences*, Vol. 27, No. 4, 2010, pp. 337–343. https://doi.org/10.5140/JASS.2010.27.4.337.

[21] Bhattacharjee, S., Kent, J. T., Faber, W. R., Hussein, I. I., and Jah, M. K., "Understanding the Effect of Perturbations on the Gaussianity of Various Coordinates for the Space Object Tracking Problem," *Proceedings of the 2018 Advanced Maui Optical and Space Surveillance Technologies Conference*, Maui, 2018.

[22] Evans, S., Taber, W., Drain, T., Smith, J., Wu, H.-C., Guevara, M., Sunseri, R., and Evans, J., "MONTE: The Next Generation of Mission Design and Navigation Software," *CEAS Space Journal*, Vol. 10, No. 1, 2018, pp. 79–86. https://doi.org/10.1007/s12567-017-0171-7.

[23] Kamiński, K., Wnuk, E., Gołębiewska, J., Krużyński, M., Kamińska, M. K., Żołnowski, M., Gędek, M., and Borek, R., "LEO Cubesats Tracking with a Network of Polish Optical SST Sensors," *Proceedings of the 2018 Advanced Maui Optical and Space Surveillance Technologies Conference*, Maui, 2018.